

Physics-Based Flow Stress Model for Alloy 718



MARIE ANNA MORETTI, LARS-ERIK LINDGREN, and PAUL ÅKERSTRÖM

A dislocation density-based model for alloy 718 in the annealed state is proposed in order to accurately describe the deformation behavior of this alloy for a wide range of thermo-mechanical loadings. The model accounts for numerous microstructural mechanisms, including strain hardening, grain size effect, dynamic strain aging (DSA), solid solution strengthening, as well as phonon and electron drag which affects dislocation movements at high strain rates. Two types of recovery mechanisms are also included: recovery due to dislocation glide and recovery associated with cross-slip of screw dislocations. The model is calibrated using experimentally determined stress-strain curves for both low and high strain rates in the order of 10^{-3} to 10^3 s^{-1} , and for temperatures in the range 20°C to 800°C . The stress-strain data computed with the model are in good agreement with the experimental data. The inclusion of DSA is found to be effective in the combination of temperatures and strain rates corresponding to experimental observations. The solid solution strengthening contribution increases with decreasing temperature and increasing strain rate. The drag effect in the model proves to be significant only for deformation at high strain rate ($\sim 10^3 \text{ s}^{-1}$).

<https://doi.org/10.1007/s11661-022-06819-7>

© The Author(s) 2022

I. INTRODUCTION

DURING manufacturing, metallic materials experience a wide range of thermo-mechanical loadings. These conditions affect the mechanical and microstructural states of the workpiece, which in turn determine its behavior in service. Thus, material constitutive relations are crucial for simulation and prediction of the deformation behavior of a workpiece during manufacturing and subsequent in-service life. This study proposes a constitutive model which can account for the evolution of the material microstructure for a nickel-based superalloy.

Mechanism-based^[1] constitutive models include microstructural information, such as grain size and solute fraction, which evolve during deformation. This coupling with microstructure aims at improving the prediction of the final mechanical and microstructural states of the material as well as the accuracy of numerical manufacturing simulations. These models also enable optimization of the manufacturing process with respect to final geometry, residual stress state and material structure.

Nickel-based superalloys are known to be excellent high temperature materials, due to their outstanding mechanical properties and good corrosion resistance. They are mainly used in the hot parts of aeroengine turbines and power plant turbine engines. Alloy 718 is the most widely used nickel-based superalloy and its deformation behavior at different thermo-mechanical loading conditions has been extensively studied in the low strain rate domain (10 s^{-1} and below). Numerous studies focus on the deformation behavior of the alloy at very high deformation temperatures, above 900°C , when recrystallization takes place in the material. In addition, several researchers investigated the dynamic strain aging (DSA) behavior of the alloy when deformed between 400°C and 700°C at low strain rates in the range of 10^{-3} to 10^{-1} s^{-1} .^[2–7] The deformation behavior of alloy 718 in the medium and high strain rate domain ($\sim 10^2 \text{ s}^{-1}$ and above) has mostly been studied at temperatures up to 800°C .^[8–14]

Research about dislocation density-based plasticity models have been published for fifty years.^[15–21] However, it is not until the last decade that they have been used in finite element simulation of manufacturing processes.^[22–25] Some authors have applied these models to alloy 718.^[26–28]

In this paper, the dislocation density-based model for alloy 718 originally proposed by Fisk *et al.*^[27] and Malmelöv *et al.*^[28] has been further developed by including dynamic strain aging, solid solution strengthening, and phonon and electron drag. The model for evolution of the density of immobile dislocations has also been extended with cross-slip. The model is

MARIE ANNA MORETTI, LARS-ERIK LINDGREN, and PAUL ÅKERSTRÖM are with the Department of Engineering Sciences and Mathematics, Luleå University of Technology, 97187 Luleå, Sweden. Contact e-mail: marie.anna.moretti@ltu.se
Manuscript submitted June 7, 2022; accepted September 6, 2022.

Article published online September 30, 2022

calibrated for a wide range of strain rates in the interval 10^{-3} to 10^3 s^{-1} and for temperatures between 20 °C and 800 °C. The model aimed to be used in finite element simulations of manufacturing processes involving high strain rates and temperatures, such as machining, but also slower processes, such as forging or rolling.

II. MATERIAL MODEL FORMULATION

Plastic deformation corresponds to the generation and movement of dislocations in the material.^[29–31] The different contributions to the flow stress can be described according to the interactions between dislocations and other microstructural features, such as other dislocations, grain boundaries or solute atoms.

The material's equivalent flow stress σ_y can be split into long-range and short-range contributions,^[16,32]

$$\sigma_y = \sigma_{\text{LR}} + \sigma_{\text{SR}}. \quad [1]$$

It is assumed that the long-range term σ_{LR} must be exceeded in order to promote macroscopic motion of dislocations across multiple grains. The short-range term σ_{SR} is the excess stress that drives dislocations past short-range obstacles and thereby maintains the plastic strain rate. The long-range and short-range terms consist of several contributions and their effects are simplified to be linearly additive.^[33]

A. Base Model for Stress Calculation

The different contributions to the material resistance against dislocation motion are assumed to be additive, as previously mentioned. In this model, the equivalent flow stress, or yield stress σ_y , is expressed as

$$\sigma_y = \sigma_G + \sigma_{\text{HP}} + \sigma_{\text{disl}} + \sigma_{\text{ss}} + \sigma_{\text{drag}}, \quad [2]$$

where σ_G is the long-range athermal stress due to interactions between dislocations that are fairly parallel to each other, σ_{HP} represents the effect of grain size, known as the Hall–Petch effect, and σ_{disl} characterizes the interaction between dislocations that are more orthogonal to each other. This part has been extended with DSA as described in Section II–B. σ_{ss} is the solid solution strengthening and σ_{drag} is the phonon and electron drag contribution. The solid solution strengthening and drag effect are new additions to this model and will be described in Sections II–C and II–D.

The long-range stress, σ_G , also referred to as the Taylor hardening, is written as^[31,34]

$$\sigma_G = \alpha M G b \sqrt{\bar{\rho}_i}, \quad [3]$$

where α is a calibration factor, M is the Taylor lattice factor, which transforms the resolved shear stress in different slip systems into an equivalent von Mises stress, G is the shear modulus of the material, b is the magnitude of the Burgers vector, and $\bar{\rho}_i$ is the mean density of immobile dislocations. The reason for

considering only the immobile dislocations for this contribution is that the density of mobile dislocations is assumed to be much smaller than the density of immobile ones.^[16] Thus, immobile dislocations provide the main contribution to strain hardening. The evolution of immobile dislocation density is described in Section II–E. In this study, the temperature-dependent shear modulus, G , and Poisson's ratio, ν , are taken from the experimental data obtained by Fukuhara and Sanpei for Inconel 718.^[35]

The Hall–Petch effect describes the effect of grain size on the material, that is, the strengthening due to grain boundaries. It is also assumed to be a long-range contribution to material resistance. Smaller grains result in more grain boundaries, which are strong dislocation barriers and increase the flow stress of fine-grained materials. Consequently, the Hall–Petch equation states that the stress associated with grain boundary hardening is inversely proportional to the average grain size. This can be formulated as^[36]

$$\sigma_{\text{HP}} = k_{\text{HP}} \frac{G}{G_{\text{RT}}} \frac{1}{\sqrt{\bar{g}}}, \quad [4]$$

where k_{HP} is the Hall–Petch parameter evaluated at room temperature, G_{RT} is the shear modulus at room temperature and \bar{g} is the average grain size. This contribution to the flow stress is scaled by the shear modulus factor in order to include a temperature dependency.

One short-range contribution to the material resistance is due to the interaction between orthogonal dislocations and is expressed as^[36,37]

$$\sigma_{\text{disl}} = f_{\text{DSA}} s_{\text{disl}} G \left(1 - \left(\frac{1}{f_{\text{DSA}} A_{\text{disl}}} \frac{k_B T}{G b^3} \ln \left(\frac{\dot{\epsilon}_{\text{ref}}}{\dot{\epsilon}_p} \right) \right)^{\frac{1}{q}} \right)^{\frac{1}{p}}, \quad [5]$$

where s_{disl} and A_{disl} are calibration parameters representing respectively the obstacle strength and the energy barrier for dislocation interactions, k_B is the Boltzmann constant, T is the absolute temperature, $\dot{\epsilon}_{\text{ref}}$ is a constant equal to 10^6 M ,^[37] $\dot{\epsilon}_p$ is the rate of equivalent plastic strain and p and q are additional parameters set to 1 in the current model. The factor f_{DSA} accounts for dynamic strain aging and is described in the next section, as a new addition to the model.

B. Dynamic Strain Aging

The parameters in Eq. [5], with $f_{\text{DSA}} = 1$, are assumed to be calibrated vs the bulk atomic fraction of solutes, X_i^{sol} . However, the solute concentration in the neighborhood of the edge dislocation may increase while it is waiting to bypass a short-range obstacle. This is assumed to increase the energy barrier according to Eq. [5]. This effect is referred to as dynamic strain aging^[38–40] and is accommodated in the model by the coefficient f_{DSA} . The introduction of this coefficient is taken from Cheng *et al.*^[41] and it is written as

Table I. Diffusion Parameters of Solutes in the Lattice

Solute	Atomic Volume [m ³] ^[37]	D_{i0}^i [m ² /s]	Q_i^i [kJ]	References
Fe	1.21×10^{-29}	3.10×10^{-5}	$280/N_A$	81
Cr	1.20×10^{-29}	2.83×10^{-5}	$276/N_A$	81
Nb	1.80×10^{-29}	5.3×10^{-7}	$236/N_A$	82

$$f_{\text{DSA}} = \sqrt{1 + \sum_i \left(\frac{X_i^{\text{sat}}}{X_i^{\text{sol}}} - 1 \right) \left(1 - e^{-\left(\frac{t_w}{t_{\text{cl}}} \right)^3} \right)}, \quad [6]$$

where i denotes a solute, X_i^{sat} is the saturation solute concentration, t_w is the waiting time of the dislocation during thermal activation and t_{cl} is the time required to diffuse to the region of interest. The atomic fractions above and below can be replaced by volumetric concentrations. The saturation concentration is written as^[41,42]

$$X_i^{\text{sat}} = X_i^{\text{sol}} \exp\left(-\frac{P\Delta V}{k_B T}\right). \quad [7]$$

The pressure, P , is taken from the continuum solution for the stress field around an edge dislocation,

$$P = \frac{Gb(1+\nu)}{3\pi(1-\nu)} \frac{\sin(\theta)}{r} = A_p \frac{\sin(\theta)}{r}, \quad [8]$$

where $A_p = \frac{Gb(1+\nu)}{3\pi(1-\nu)}$. P is evaluated at a distance $r = 3b$ above or below the dislocation ($\theta = \pm\pi/2$). ΔV is the difference between the atomic volume of the solute and that of the host lattice, ω .^[42]

The waiting time can be derived from the thermal activation model,^[41]

$$t_w = \frac{\dot{\epsilon}_{\text{ref}}}{\vartheta_a \dot{\epsilon}_p}, \quad [9]$$

where ϑ_a is the attempt frequency. Shoenck^[43] estimated it for a dislocation segment as a fraction of the Debye frequency ϑ_D , so that $\vartheta_a = 10^{-3}\vartheta_D$. $\dot{\epsilon}_{\text{ref}}$ is the same constant as in Eq. [5].

The characteristic time, related to the diffusion, is given by^[44]

$$t_{\text{cl}} = b^3 \sqrt{\frac{2}{\pi}} \frac{k_B T}{A_p \Delta V D_i^i} \left(\frac{X_i^{\text{sat}}}{3X_i^{\text{sol}}} \right)^{3/2}, \quad [10]$$

where D_i^i is the diffusivity of solute i in the lattice, obtained from

$$D_i^i = \frac{X_v}{X_v^{\text{eq}}} D_{i0}^i \exp\left(-\frac{Q_i^i}{k_B T}\right), \quad [11]$$

where D_{i0}^i is the pre-exponential diffusion parameter for the solute and Q_i^i is the activation energy for solute diffusion. The pre-exponential diffusion parameter is

evaluated under equilibrium vacancy concentration X_v^{eq} . The diffusivities of substitutional solutes are scaled by X_v/X_v^{eq} , where $X_v > X_v^{\text{eq}}$ is the excess vacancy concentration. The excess vacancies are evaluated using the model proposed by Militzer *et al.*^[45] Three solutes are taken into account in the DSA model: iron, chromium and niobium. The diffusivity parameters for these solutes are given in Table I, where N_A is the Avogadro number.

C. Solid Solution Strengthening

Substitutional or interstitial solutes in the crystal lattice interact with the dislocations and, in most cases, contribute to the strength of the material. In this work, the model for solid solution strengthening is based on the work of Varvenne *et al.*^[46] and Leyson *et al.*,^[47,48] following the approach initially proposed by Labusch.^[49] The solute hardening is a short-range contribution to the flow stress. For a solute i , it can be written as

$$\sigma_{ss,i} = \sigma_{ss0} \exp\left(-\frac{1}{C_1} \frac{k_B T}{\mathcal{H}_{\text{sol}}} \ln\left(\frac{\dot{\epsilon}_{ss}}{\dot{\epsilon}_p}\right)\right), \quad [12]$$

where C_1 is a fitting parameter equal to 0.57016 (see Appendix A) and $\dot{\epsilon}_{ss}$ is a reference strain rate set to 10^5 s^{-1} .

σ_{ss0} is a factor expressed as

$$\sigma_{ss0} = A_L M G \left(\frac{1}{4\pi^2 N_{\text{cell}}} \right)^{4/3} \left(\frac{w}{b} \right)^{1/3} (\epsilon_i^{\text{mis}})^{4/3} (X_i^{\text{sol}})^{2/3}, \quad [13]$$

with $A_L = 1/\sqrt{2}$. N_{cell} is the number of atoms in a unit cell, which is equal to 4 for a face-centered cubic lattice. w is the range of action of a diffuse obstacle estimated to $\frac{w}{b} = 1.7$.^[50] X_i^{sol} is the atomic fraction of the alloying element i and ϵ_i^{mis} is the misfit due to this element, which depends on both the size and modulus misfit, according to,^[51]

$$\epsilon_i^{\text{mis}} = \alpha \delta_i + \eta'_i, \quad [14]$$

where $\eta'_i = \eta_i / (1 + |\eta_i|/2)$ with η_i the shear modulus misfit of the solute i . α is a factor set to 16^[52,53] and δ_i is the size misfit of the solute i . The shear modulus and size misfits of the different solutes are shown in Appendix A.

The energy barrier \mathcal{H}_{sol} is expressed as

$$\mathcal{H}_{\text{sol}} = 5.55 G b^3 \left(\frac{w}{b} \right)^{3/2} \sqrt{\frac{\sigma_{ss0}}{M G}}. \quad [15]$$

The total solid solution strengthening contribution is obtained by summation of the individual solute contributions as

$$\sigma_{ss} = \left(\sum_i \sigma_{ss,i}^{3/2} \right)^{2/3}. \quad [16]$$

D. Phonon and Electron Drag

During high strain rate deformation ($\sim 10^3 \text{ s}^{-1}$ and above), phonon and electron interact with dislocations moving at high speed and induce a drag force which reduces the dislocation velocity. This is a short-range contribution to the flow stress and it is expressed as^[37]

$$\sigma_{\text{drag}} = M^2 G \left(\frac{B_p}{B_0} + \frac{T}{300} \right) \dot{\epsilon}_p, \quad [17]$$

where B_p and B_e are respectively the phonon and electron drag parameters to be calibrated, and B_0 is an additional calibration parameter.

In addition, high speed deformations do not allow sufficient time for heat dissipation, leading to a temperature rise in the material, known as adiabatic heating. This effect is included in the model for high strain rate deformation. The temperature increase ΔT for an applied stress σ after a strain ϵ is written as^[13,54]

$$\Delta T = \frac{\eta_{\text{TQ}}}{\rho C_s} \int_0^\epsilon \sigma d\epsilon, \quad [18]$$

where η_{TQ} is the Taylor-Quinney factor, set to a constant value of 0.9. ρ is the density of the material. C_s is the specific heat capacity, for which temperature-dependent data for alloy 718 are taken from Agazhanov *et al.*^[44]

E. Dislocation Density Evolution

The immobile dislocation density $\bar{\rho}_i$ is involved in the calculation of the Taylor hardening stress contribution σ_G , Eq. [3]. Its evolution $\dot{\bar{\rho}}_i$ is associated with the hardening and softening of the material. It can be written as

$$\dot{\bar{\rho}}_i = \dot{\bar{\rho}}_i^{(+)} + \dot{\bar{\rho}}_i^{(-)}, \quad [19]$$

where $\dot{\bar{\rho}}_i^{(+)}$ and $\dot{\bar{\rho}}_i^{(-)}$ describe the hardening and softening effects, respectively.

Strain hardening in a material is characterized by an increase in the immobile dislocation density. The rate at which the immobile dislocation density ρ_i is increased may be written as^[16]

$$\dot{\bar{\rho}}_i^{(+)} = \frac{M \dot{\epsilon}_p}{b \bar{\Lambda}}, \quad [20]$$

where $\bar{\Lambda}$ is the mean free path, which corresponds to the distance covered by mobile dislocations before

being immobilized by obstacles. It can be computed from the contributions of different obstacles according to

$$\frac{1}{\bar{\Lambda}} = \left(\frac{1}{\bar{g}} + \frac{1}{\bar{s}} \right), \quad [21]$$

where \bar{g} and \bar{s} are the mean grain size and sub-grain size, respectively. The mean sub-grain size can be calculated using a relation proposed by Holt,^[55]

$$\bar{s} = \frac{K_c}{\sqrt{\bar{\rho}_i}}. \quad [22]$$

K_c is a parameter adapted from Galindo-Nava and Rivera-Díaz-del-Castillo,^[56] ignoring its direct temperature dependency. The factor is taken as

$$K_c = C_{\text{cell}} \frac{12\pi(1-\nu)}{2+\nu}, \quad [23]$$

where C_{cell} is a calibration parameter.

Recovery is a softening process involving rearrangement and annihilation of dislocations, thus leading to a reduction of the dislocation density. This mechanism is expressed as

$$\dot{\bar{\rho}}_i^{(-)} = \dot{\bar{\rho}}_i^{(-)(cs)} + \dot{\bar{\rho}}_i^{(-)(gl)}, \quad [24]$$

where $\dot{\bar{\rho}}_i^{(-)(cs)}$ and $\dot{\bar{\rho}}_i^{(-)(gl)}$ correspond to the evolution of immobile dislocation density related to recovery due to cross-slip and glide, respectively.

Cross-slip of screw dislocations activates additional slip systems and the probability of cross-slip increases with stress and temperature. The evolution of immobile dislocation density due to cross-slip is expressed as

$$\dot{\bar{\rho}}_i^{(-)(cs)} = \Omega_p \frac{15 \bar{d}_{\text{SFE}}}{L_{cs}} \left(\frac{\sigma}{MG} \right)^2 \vartheta_D e^{-\frac{\Omega_{cs} Q_{cs}}{k_B T}} \bar{\rho}_i H(\dot{\epsilon}_p), \quad [25]$$

where Ω_p and Ω_{cs} are calibration parameters, σ is the equivalent von Mises stress and $H(\dot{\epsilon}_p)$ is the Heaviside step function. The mean width of the stacking fault for a screw dislocation is $\bar{d}_{\text{SFE}} = \frac{Gb^2}{24\pi\gamma_{\text{SFE}}} \frac{2-3\nu}{1-\nu}$, where γ_{SFE} is the surface energy of the stacking fault. $L_{cs} =$

$l_c \bar{d}_{\text{SFE}} \sqrt{\ln(10^4)}$ is the length of the initial cross-slipping dislocation segment, with l_c the non-dimensional characteristic length. Q_{cs} is the calibrated activation energy for cross-slip. Derivation of the cross-slip model and expression for l_c and Q_{cs} are given in Appendix B.

Recovery due to glide is associated with annihilation of immobile dislocations by the mobile ones. It is expressed based on the formulation by Bergström^[16] as

$$\dot{\bar{\rho}}_i^{(-)(gl)} = \Omega_0 \bar{\rho}_i \dot{\epsilon}_p, \quad [26]$$

where Ω_0 is a calibration parameter.

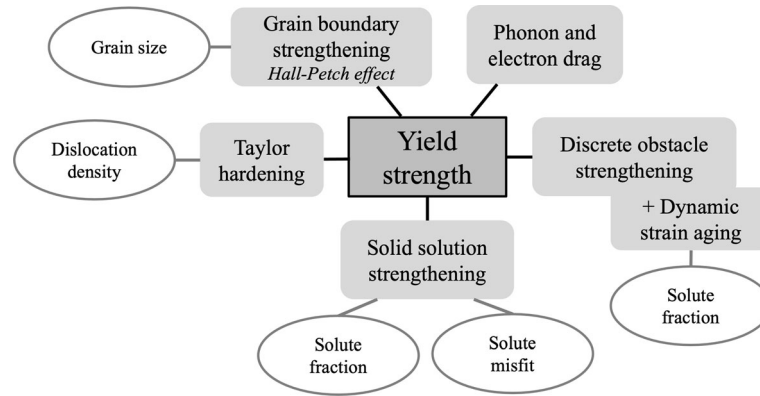


Fig. 1—Schematic representation of the different contributions to yield strength in the model.

F. Stress Update

The model is implemented in the context of von Mises associated plasticity with isotropic hardening. The increment in equivalent plastic strain is computed using a radial return algorithm in order to stay on the yield surface during plastic straining. The latter means that the yield stress is calculated according to Eq. [2] and this must be equal to the equivalent von Mises stress. The increment in equivalent plastic strain is solved by a Newton–Raphson iterative method requiring a plastic hardening modulus evaluated as:

$$H' = \frac{\partial \sigma_G}{\partial \bar{\rho}_i} \frac{\partial \bar{\rho}_i}{\partial \epsilon_p} + \frac{\partial \sigma_{disl}}{\partial \epsilon_p} + \frac{\partial \sigma_{ss}}{\partial \epsilon_p} + \frac{\partial \sigma_{drag}}{\partial \epsilon_p} \\ = \frac{\partial \sigma_G}{\partial \bar{\rho}_i} \frac{\partial \bar{\rho}_i}{\partial \epsilon_p} + \frac{1}{\Delta t} \left(\frac{\partial \sigma_{disl}}{\partial \dot{\epsilon}_p} + \frac{\partial \sigma_{ss}}{\partial \dot{\epsilon}_p} + \frac{\partial \sigma_{drag}}{\partial \dot{\epsilon}_p} \right), \quad [27]$$

where Δt is the time step. The immobile dislocation density, Eq. [19], is computed for each time step using an implicit iterative algorithm.

Figure 1 summarizes the different contributions to the yield stress as implemented in the model according to Eq. [2], and illustrates the microstructural features influencing each contribution.

III. MODEL CALIBRATION AND VALIDATION

The model was calibrated using compression tests data for alloy 718 in annealed state. The composition of the alloy is presented in Table II. The material was solution annealed by maintaining it at 950 °C for 1 hour, resulting in the absence of γ' and γ'' precipitates.^[57] The material parameters and constants collected from the literature and used in the current study are listed in Table III.

The calibration parameters were first calibrated in the low strain rate domain (1 s^{-1} and below), according to the experimental results obtained by Fisk *et al.*^[27] In this case, the average grain size was set to 20 μm . An initial calibration was performed using experimental flow stress curves at a strain rate of 1 s^{-1} for the temperatures 35 °C, 200 °C, 400 °C, 600 °C, 700 °C and 800 °C.

For the high strain rate domain ($1000\text{--}4000 \text{ s}^{-1}$), compression tests were performed using a Split-Hopkinson pressure bar device in a previous study.^[58] For those tests, the average grain size was measured to 15 μm using scanning electron microscopy coupled with electron backscatter diffraction (EBSD) technique. Stress–strain curves for the strain rates 1400 and 2000 s^{-1} at 20 °C, 400 °C and 800 °C were used for calibration of the phonon and electron drag parameters included in Eq. [17].

The model calibration was performed by an error minimization procedure using a MATLAB-based toolbox. This toolbox uses a constrained nonlinear optimization routine which allows calibration using flow stress data from multiple experiments conducted at different temperatures and strain rates. Table IV summarizes the final optimized parameters. Figures 2 and 3 illustrate the calibration results for the different strain rates and temperatures used.

The calibration shown in Figures 2 and 3 gives parameters for which the model achieves a fair agreement to the flow stress behavior given by the experiments. The major discrepancy for the higher temperatures is commented on in Section IV.

The elastic properties are set constant during the calibration and taken from literature. This physics-based model utilizes the elastic parameters, which means that if better values for elastic properties are found, then the calibration parameters must be adjusted accordingly or recalibrated. The data at small strains in the experimental curves are limited and less precise than at high strains. Therefore, the agreement between model and experiment is varying at small strains.

The model with the calibrated parameters was validated for different compressive loadings shown in Figures 4 and 5. Overall, the stress–strain results of the model are in good accordance with the experimental results. One should note that the experimental results cannot be considered as exact. For example, at a strain of 0.5, the test at 35 °C with rate 1 s^{-1} has a lower stress than the case 50 °C with rate 0.01 s^{-1} .

Table II. Chemical Composition of Alloy 718 Material Used in This Study

Element	Ni	Fe	Cr	Nb	Mo	Ti	Al
Wt. Pct	49.62 ± 1.35	17.58 ± 0.49	17.18 ± 0.49	4.75 ± 0.20	2.58 ± 0.12	1.08 ± 0.06	0.43 ± 0.05

Table III. Model Parameters from the Literature

Symbol	Physical Meaning	Unit	Value	References
a_γ	lattice parameter for the γ -phase (matrix)	m	3.52×10^{-10}	83
b	magnitude of the Burgers vector	m	2.54×10^{-10}	27, 84
D_{v0}	pre-exponential parameter for self-diffusion	m^2/s	1.6×10^{-4}	37
G	temperature-dependent shear modulus	MPa	—	35
G_{RT}	shear modulus at room temperature	MPa	80.77×10^3	35
k_B	Boltzmann constant	J/K	1.38×10^{-23}	—
k_{HP}	Hall–Petch coefficient	MPa $\text{m}^{1/2}$	0.35×10^6	adapted from 85
M	Taylor lattice factor (for face-centered cubic metals)	—	3.06	37
N_A	Avogadro constant	mol^{-1}	6.022×10^{23}	—
Q_v	activation energy for self-diffusion	kJ	$285/N_A$	37
γ_{SFE}	stacking fault energy	J/m ²	0.075	86
ϑ_D	Debye frequency	rad/s	9.88×10^{13}	87
ν	temperature-dependent Poisson’s ratio	—	—	35
ρ	density at room temperature	kg/m ³	8193	88
ω	atomic volume $-\omega = a^3/4$	m ³	1.09×10^{-29}	—

Table IV. Calibrated Parameters

Symbol	Description	Equation	Value
A_{disl}	Calibration parameter in the expression of σ_{disl}	(5)	1
B_e	Electron drag parameter	(17)	$\frac{B_e}{B_p} = 0.1$
B_p	Phonon drag parameter	(17)	
B_0	Calibration parameter in the expression of σ_{drag}	(17)	$7 \cdot 10^6$
C_{cell}	Calibration parameter for K_c in the expression of $\bar{\epsilon}$	(22)	3.75
s_{disl}	Calibration factor in the expression of σ_{disl}	(5)	$1.5 \cdot 10^{-3}$
α	Calibration factor in the expression of σ_G	(3)	0.5
Ω_{cs}	Calibration parameter for the cross-slip activation energy Q_{cs}	(25)	0.7
Ω_p	Calibration parameter for cross-slip	(25)	15
Ω_0	Calibration parameter for recovery by glide	(26)	8.4
ρ_{i0}	Initial immobile dislocation density (m^{-2})	—	$1.5 \cdot 10^{11}$

IV. DISCUSSION

The proposed dislocation density-based model has been adapted for alloy 718 based on the work by Lindgren *et al.*^[36] for AISI 316 L and Fisk *et al.*^[27] for alloy 718. Several additions and modifications have been made to improve the model. The main ones are recovery by cross-slip, dynamic strain aging, solid solution strengthening, and phonon and electron drag. Each of them is discussed in this section.

A. Cross-Slip

The cross-slip model is found to be able to represent the sudden reduced hardening for higher temperatures. The hardening becomes very small after some cross-slip and this effect increases with decreasing strain rate according to Figures 2, 4 and 5. The model does not provide abrupt change in behavior when increasing the temperature from 700 °C to 800 °C, as seen in Figures 2 and 4. The behavior of the model for various strain rates is illustrated in Figure 6.

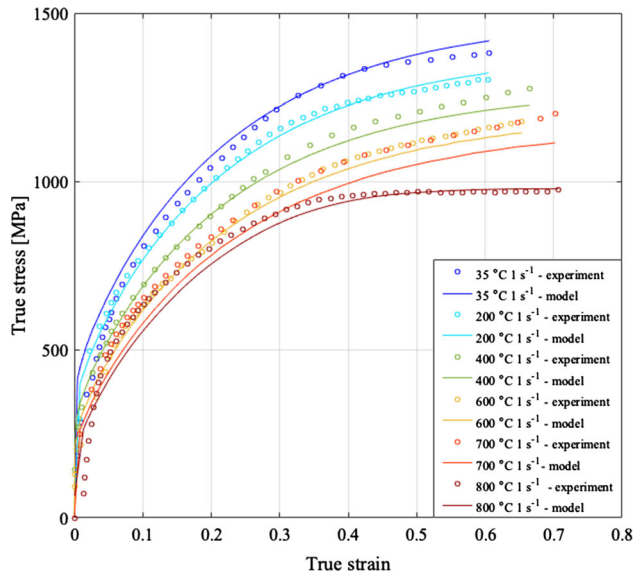


Fig. 2—Model calibration using the true stress–strain curves obtained experimentally at 1 s^{-1} .

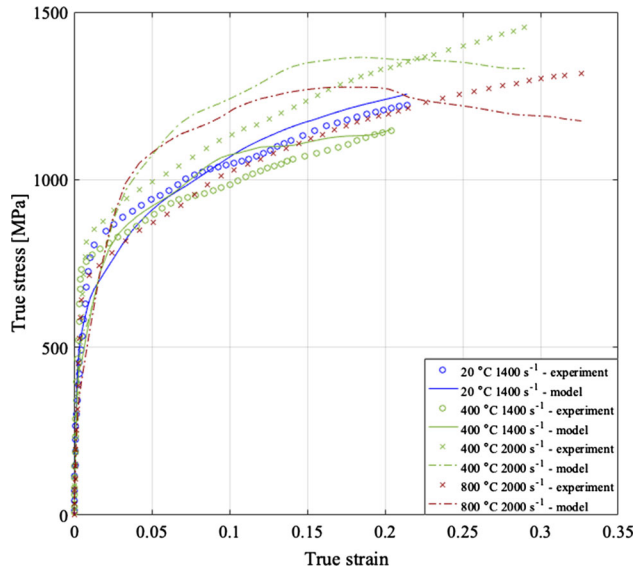


Fig. 3—Model calibration using the true stress–strain curves obtained experimentally at high strain rates ($\sim 10^3 \text{ s}^{-1}$).

B. Dynamic Strain Aging

DSA has been observed to be an active mechanism in alloy 718 for deformation at a strain rate below 0.1 s^{-1} and temperatures between 200 °C and 750 °C .^[2–4,6,26,59–63] In this work, the effect of DSA in a physics-based flow stress model has been included, according to Section II–B.

The results for 0.01 s^{-1} (Figure 4) presents a similar flow stress at 400 °C and 600 °C , suggesting that the DSA is accounted for in the model. Overall, the results are in good agreement with the mechanical tests results. It can be noted that the experimental stress–strain data have been smoothed for calibration purpose, but the original curve at 600 °C is heavily serrated,

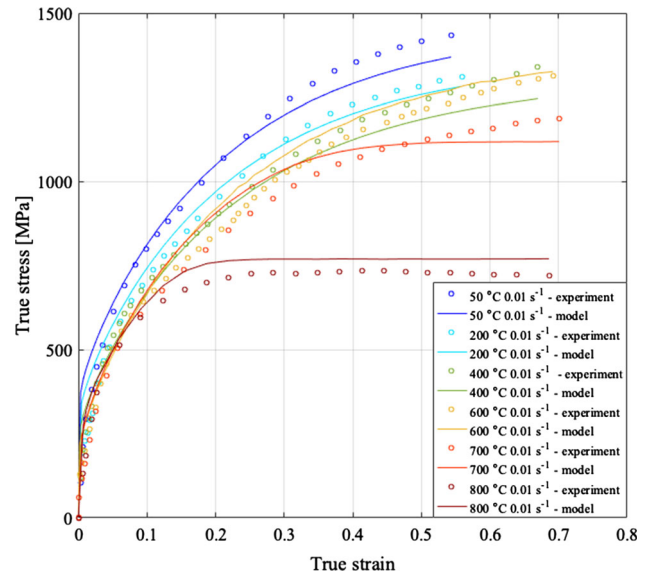


Fig. 4—Model validation for true stress–strain curves obtained experimentally at 0.01 s^{-1} .

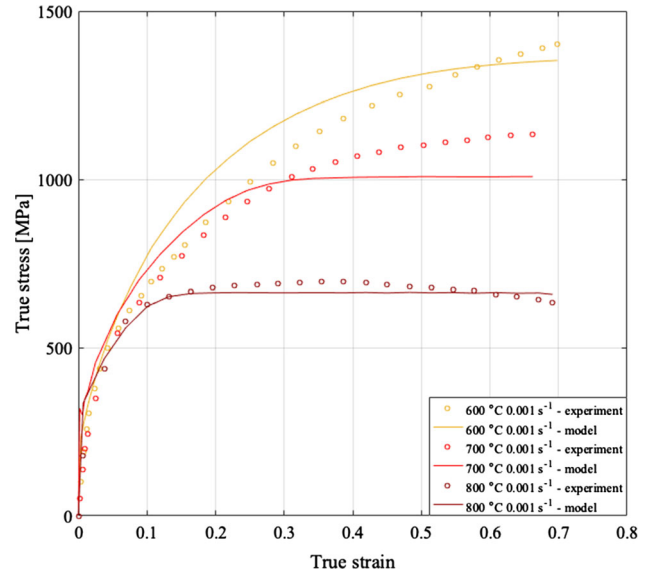


Fig. 5—Model validation for true stress–strain curves obtained experimentally at 0.001 s^{-1} .

corresponding to the DSA-related Portevin–Le Chatelier effect,^[6] as it can be seen in Figure 7.

Figure 8 shows the effect for various strain rates at 600 °C . The higher rates have a lower flow stress. The flow stress is overpredicted initially for the lowest strain rate, 0.001 s^{-1} . This is due to the model giving a large initial increase in f_{DSA} for this case according to Figure 9.

C. Solid Solution Strengthening

The solid solution strengthening contribution σ_{ss} , Eq. [16], computed using the model, is presented in Figure 10 for different temperatures and strain rates.

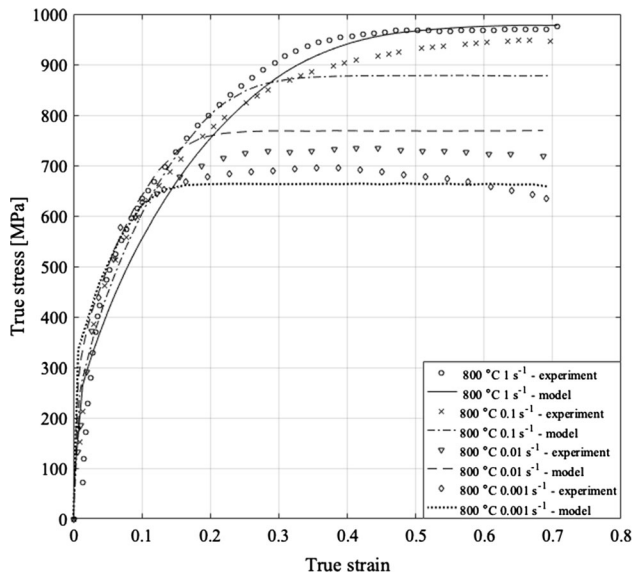


Fig. 6—Illustration of effect of cross-slip at 800 °C for various strain rates.

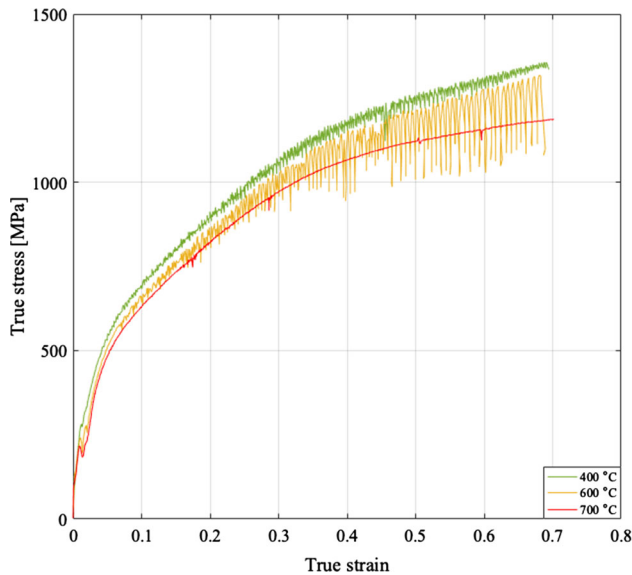


Fig. 7—Raw experimental data for true stress-strain curve at 0.01 s^{-1} .

The deformation temperature is fairly constant during each test. The strain rate presents small initial variations for the low strain rate tests (1 s^{-1} and below), but it varies significantly throughout the deformation at high strain rate ($\sim 10^3 \text{ s}^{-1}$).^[58] This last feature explains the small variations in the solute contribution in the high strain rate domain. Furthermore, the solid solution strengthening decreases when the deformation temperature increases. Physically, it corresponds to the greater dislocation mobility at higher temperatures due to increased diffusivity. On the contrary, the solid solution strengthening contribution increases with increasing strain rate, as the resistance to dislocation motion increases with their speed.

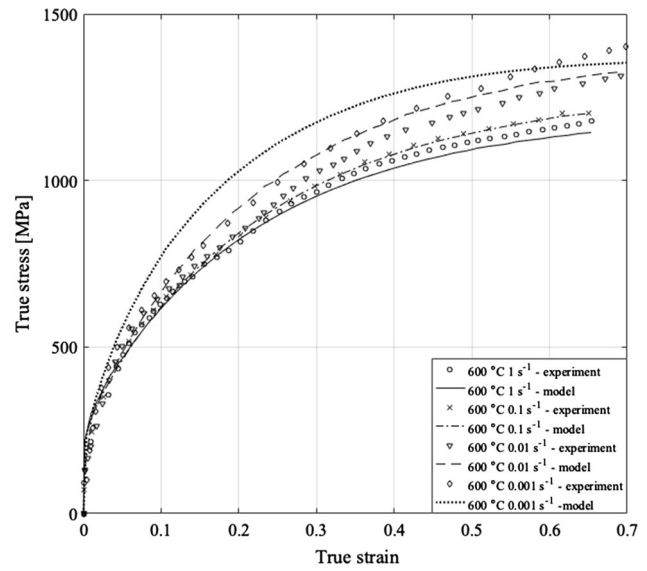


Fig. 8—Effect of DSA at 600 °C.

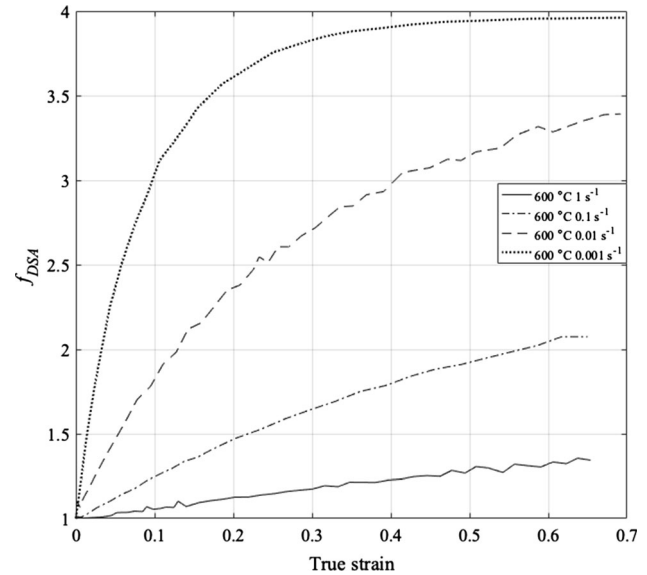


Fig. 9—Evolution of DSA factor, f_{DSA} in Eq. [6], with respect to true strain.

D. Phonon and Electron Drag

The phonon and electron drag, described in Section II–D, is a mechanism that is expected to be active during deformation at high strain rate. Figure 11 shows the drag stress contribution computed using the model.

The phonon and electron drag in the model is negligible at low strain rate (1 s^{-1} and below) compared to the high strain rate deformation ($\sim 10^3 \text{ s}^{-1}$), which validates the use of this formulation. According to Eq. [17], the drag stress contribution increases with both strain rate and temperature. Phonons correspond to thermal vibration in the crystal lattice. Thus, at higher temperature, there are more phonons to disturb the motion of dislocations.

The model exhibits a reduction in flow stress from a strain of approximately 0.2 (Figure 3) and a

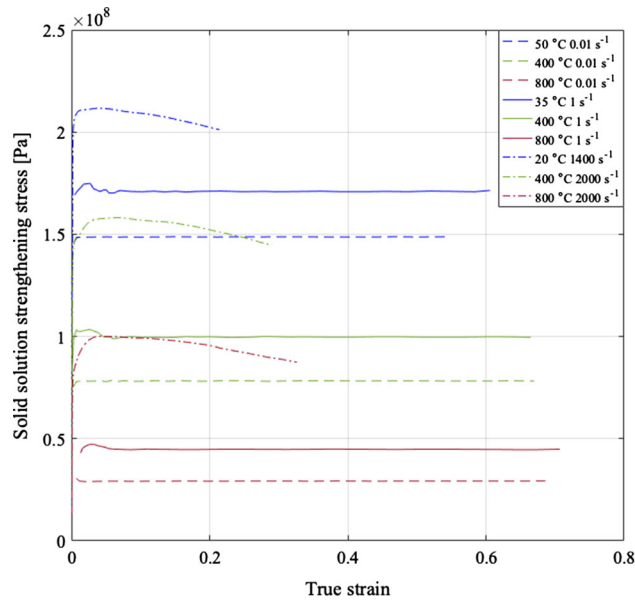


Fig. 10—Solid solution strengthening contribution σ_{ss} with respect to true strain.

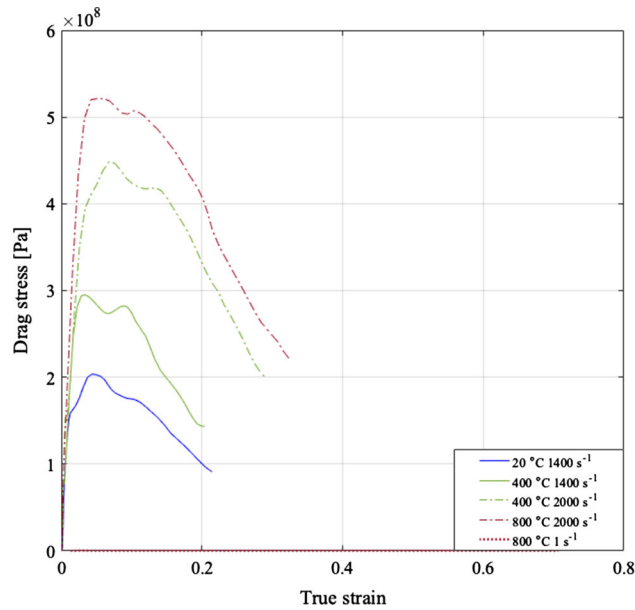


Fig. 11—Phonon and electron drag contribution σ_{drag} with respect to true strain.

corresponding decrease in drag stress, as shown in Figure 11. This is attributed to a decrease in the evaluated strain rate, as illustrated in Figure 12.

V. SUMMARY AND CONCLUSION

A physics-based flow stress model for alloy 718 in annealed state has been proposed.

The long-range stress contributions in the model are:

- Taylor hardening, corresponding to the interaction between dislocations in a same plane.

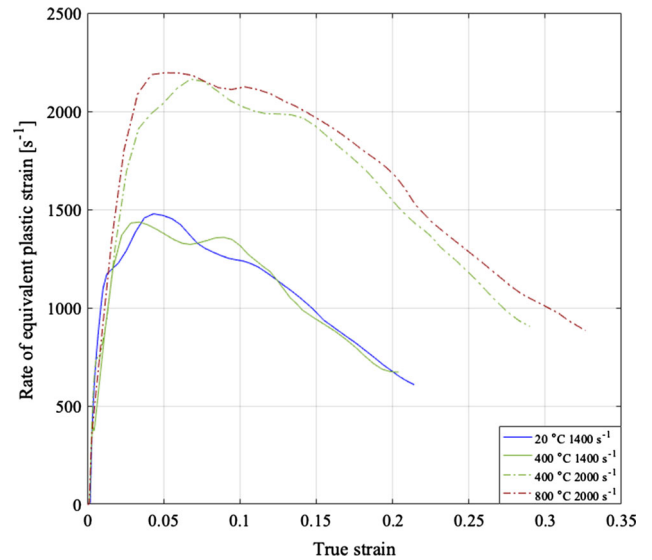


Fig. 12—Evaluated rate of equivalent plastic strain.

- Grain boundary strengthening (Hall–Petch effect). The short-range stresses, assisted by thermal activation, are:
- Discrete obstacle contribution, corresponding to the interaction between gliding dislocation and discrete obstacles in the matrix. This contribution also includes the effect of DSA.
- Solid solution strengthening.
- Phonon and electron drag.

The evolution of immobile dislocation density includes the following mechanisms.

- Strain hardening, related to the increase in immobile dislocation density.
- Recovery by cross-slip of screw dislocations.
- Recovery by dislocation glide.

The model has been calibrated and validated for both low and high strain rates (10^{-3} to 10^3 s^{-1}) for temperatures between 20 °C and 800 °C. The predicted flow stresses are in good agreement with the experimental results. In addition, it was shown that the addition of cross-slip and DSA improves the accuracy of the flow stress prediction, and the addition of the drag stress enables the model to also fit the high strain rate deformation behavior.

In order to accommodate deformation temperatures above 900 °C, a recrystallization model is required.^[8,56,58,64–71] In addition, in order to extend the predictions to aged alloy 718, which is widely used in the industry, the precipitation model proposed by Fisk *et al.*^[27] can be added.

ACKNOWLEDGMENTS

This research work is a part of the European Network for Alloys Behaviour Laws Enhancement (ENABLE) project funded by the European Union's Marie Skłodowska–Curie Actions (MSCA) Innovative

Training Networks (ITN) H2020- MSCA-ITN-2017 under the grant Agreement No. 764979. Lars-Erik Lindgren acknowledges the financial support of strategic innovation program for lightweight provided by VINNOVA, Formas and Energimyndigheten. Furthermore, the authors would like to thank Dr. Martin Fisk for providing the experimental data.

CONFLICT OF INTEREST

On behalf of all authors, the corresponding author states that there is no conflict of interest.

FUNDING

Open access funding provided by Lulea University of Technology.

OPEN ACCESS

This article is licensed under a Creative Commons Attribution 4.0 International License, which permits use, sharing, adaptation, distribution and reproduction in any medium or format, as long as you give appropriate credit to the original author(s) and the source, provide a link to the Creative Commons licence, and indicate if changes were made. The images or other third party material in this article are included in the article’s Creative Commons licence, unless indicated otherwise in a credit line to the material. If material is not included in the article’s Creative Commons licence and your intended use is not permitted by statutory regulation or exceeds the permitted use, you will need to obtain permission directly from the copyright holder. To view a copy of this licence, visit <http://creativecommons.org/licenses/by/4.0/>.

APPENDIX A: SOLID SOLUTION STRENGTHENING CALCULATION

Alloy 718 is a nickel-based superalloy with Cr atoms in substitution in the Ni matrix (γ -phase). The alloy benefits from the solid solution Ni–Cr strengthening properties. Then, in the contribution of solid solution strengthening to the flow stress σ_{ss} , Eq. [12], the parameter C_1 was calibrated according to data for different concentrations of chromium in nickel obtained from Akhtar and Teghtsoonian.^[72] The value of C_1 was fitted to 0.57016 and the calibration result is shown in Figure A1. This value was used for all the solutes included in the solute hardening model in this work.

In addition to Cr, other interstitial or substitutional atoms increase the alloy strength. The contribution of solid solution hardening to the flow stress is described in Section II–C and its calculation requires data for the solute misfit, Eqs. [13] and [14]. The size misfit δ_i for the solute i is calculated as

$$\delta_i = \frac{1}{a_\gamma} \frac{da}{dX_i^{\text{sol}}}, \tag{A1}$$

with a_γ the reference lattice parameter, which is the lattice parameter of the matrix ($a_\gamma = 3.52 \text{ \AA}$). da/dX_i^{sol} is the variation of the lattice parameter with respect to the atomic fraction of the solute, which is computed according to the results obtained by Akhtar and Teghtsoonian^[72] for Cr and by Mishima *et al.*^[73] for the other solutes.

The shear modulus misfit η_i for the solute i is calculated as

$$\eta_i = \frac{1}{G_{\text{RT}}} \frac{dG}{dX_i^{\text{sol}}}, \tag{A2}$$

where G_{RT} is the shear modulus of the material at room temperature ($G_{\text{RT}} = 80.77 \text{ GPa}$). $dG/dX_i^{\text{sol}} = 2(1 + \nu)dE/dX_i^{\text{sol}}$ is the variation in shear modulus with respect to the atomic fraction of the solute, with ν the Poisson’s ratio and E the Young’s modulus. It is calculated using the results obtained by Karmazin^[74] for Cr and by Mishima *et al.*^[75] for the other solutes.

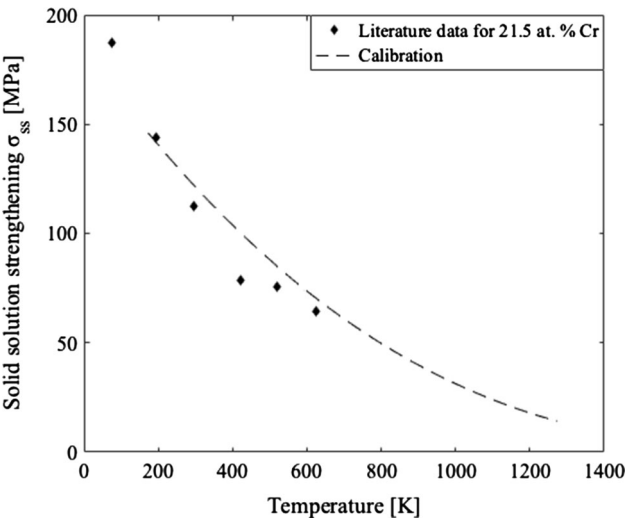


Fig. A1—Evolution of solid solution strengthening contribution σ_{ss} with temperature after calibration of parameter C_1 using experimental data from Akhtar and Teghtsoonian^[72].

Table A1. Size and Shear Modulus Misfit of Cr in Ni

Solute	Size Misfit δ	Shear Modulus Misfit η	Reference for Calculation
Cr	0.0298	1.7541	72, 74
Nb	0.1978	– 1.3928	73, 75
Al	0.0513	– 0.0952	73, 75
Ti	0.1193	– 1.8261	73, 75
Mo	0.1349	– 0.1190	73, 75
Fe	0.0333	– 1.2380	73, 75
W	0.0125	1.3618	73, 75
Mn	0.0823	– 2.0737	73, 75

Table A1 presents data for solute size misfit δ and shear modulus misfit η .

APPENDIX B: CROSS-SLIP RECOVERY MODEL

This Appendix explains the derivation of the cross-slip model presented in Eq. [25].

Argon treated recovery by cross-slip as dynamic recovery,^[76]

$$\dot{\bar{\rho}}_i^{(-)(cs)} = C_{Argon} P_{cs} \bar{\rho}_i \dot{\gamma}^p, \quad [B1]$$

with $\bar{\rho}_i$ the density of immobile dislocation and $\dot{\gamma}^p$ the plastic shear rate. The probability for cross-slip P_{cs} may be taken as the Boltzmann factor $e^{-\frac{Q_{cs}}{k_B T}}$, with Q_{cs} the activation energy for cross-slip. The coefficient C_{Argon} may be taken as the product of the frequency of attempts Γ_{cs} and a characteristic time τ_{cs} for the dislocation about to cross-slip, leading to

$$\dot{\bar{\rho}}_i^{(-)(cs)} = \tau_{cs} \Gamma_{cs} e^{-\frac{Q_{cs}}{k_B T}} \bar{\rho}_i \dot{\gamma}^p H(\dot{\gamma}^p), \quad [B2]$$

The Heaviside function $H(\dot{\gamma}^p)$ is introduced, as the plastic shear rate will be canceled by a characteristic time later in the derivation and the cross-slip occurs only when dislocations glide. The attempt frequency for a dislocation segment is taken from Shoenck^[43] as

$$\Gamma_{cs} = \vartheta_D \frac{b}{L_{cs}}, \quad [B3]$$

where L_{cs} is the length of the cross-slipping dislocation segment given later in this appendix.

The characteristic time for cross-slip is estimated as

$$\tau_{cs} = \frac{\bar{d}_{SFE}}{\bar{v}} = \frac{\bar{d}_{SFE}}{\dot{\gamma}^p / b \rho_m}. \quad [B4]$$

The mean width of the stacking fault for a screw dislocation, \bar{d}_{SFE} , is

$$\bar{d}_{SFE} = \frac{Gb^2}{24\pi\gamma_{SFE}} \frac{2-3\nu}{1-\nu}. \quad [B5]$$

The relation between dislocation mean velocity and plastic shear rate is taken from^[77] giving

$$\tau_{cs} = \frac{\bar{d}_{SFE}}{\bar{v}} = \frac{15\bar{d}_{SFE}}{b} \left(\frac{\tau_{SR}}{G} \right)^2 \frac{1}{\dot{\gamma}^p}. \quad [B6]$$

τ_{SR} is the shear stresses corresponding to the short-range terms in Eq. [2]. It is the sum of the interactions between dislocations, solid solution strengthening and phonon and electron drag contributions. This is the excess stress driving the dislocations. Inserting this into Eq. [B2] leads to an expression like static recovery, as the strain rate disappears,

$$\dot{\bar{\rho}}_i^{(-)(cs)} = \frac{15\bar{d}_{SFE}}{b} \left(\frac{\tau_{SR}}{G} \right)^2 \frac{b}{L_{cs}} \vartheta_D e^{-\frac{Q_{cs}}{k_B T}} \bar{\rho}_i H(\dot{\gamma}^p). \quad [B7]$$

The enthalpy barrier Q_{cs} decreases with the applied shear stress. Kuykendall *et al.*^[78] noted that Kubin *et al.*^[79] proposed that the Schmid stress on the original glide plane is the most important stress component. It is therefore written as

$$Q_{cs} = Q_{cs0} - \tau V_{act} = Q_{cs0} - \tau b L_{cs} \bar{d}_{SFE}, \quad [B8]$$

where τ is the applied stress resolved according to the slip direction which drives the dislocation on the initial slip plane. It is called the Schmid stress. V_{act} is the activation volume for the model.

There is also driving shear stress on the cross-slip plane included by Markovitz and Mordehai^[80] giving an additional stress reduction included in Q_{cs0} . There are three characteristic dimensions. One is the mean width of the stacking fault \bar{d}_{SFE} given by Eq. [B5]. The second is the distance over which the partials bend,

$$\lambda_{SFE} = \frac{1}{2} \bar{d}_{SFE} \sqrt{\ln \left(\frac{R}{r_0} \right)}, \quad [B9]$$

where the outer and inner external cut-off radii, R and r_0 , are the ranges over which the energy in the continuum dislocation model is integrated. The former is the outer radius related to distance to neighboring dislocations and the latter is the core radius within which the continuum model is invalid. Markovitz and Mordehai^[80] assumed that R is four orders of magnitude larger than r_0 giving $\lambda_{SFE} = \frac{1}{2} \bar{d}_{SFE} \sqrt{\ln(10^4)}$. Their final model led to

$$Q_{cs0} = 3.10 \gamma_{SFE} \lambda_{SFE} \bar{d}_{SFE}. \quad [B10]$$

They also derived the third characteristic length, which is the length of the cross-slipping dislocation segment. It is given by

$$L_{cs} = 2l_c \lambda_{SFE}. \quad [B11]$$

where the critical non-dimensional length l_c is obtained by solving

$$\frac{1.55}{(\cosh(l_c))^2} - 3\delta l_c^2 = 0. \quad [B12]$$

The parameter δ is defined as

$$\delta = \frac{1}{6} \left(\frac{b \tau_{cs}^{Schmid}}{\lambda_{SFE}} \right)^2, \quad [B13]$$

where τ_{cs}^{Schmid} is the Schmid stress in the cross-slip plane. Insertion of this into Eq. [B12] leads to

$$\frac{1.55}{(\cosh(l_c))^2} - \frac{1}{2} \left(\frac{b \tau}{\lambda_{SFE}} \right)^2 l_c^2 = 0. \quad [B14]$$

The subscript and superscripts on the shear stress are ignored, as the developed model will only use one shear stress. This inclusion leads to a reduction of the activation enthalpy as

$$Q_{cs} = Q_{cs0} f_{lc}(\tau) - \tau b L_{cs} \bar{d}_{SFE}, \quad [\text{B15}]$$

where

$$f_{lc}(\tau) = \frac{1}{2} \left[1 + \tanh(l_c) - \frac{1}{6} \left(\frac{b\tau}{\lambda_{SFE}} \right)^2 \frac{(0.6l_c)^3}{1.55} \right]. \quad [\text{B16}]$$

REFERENCES

- H.J. Frost and M.F. Ashby: Deformation-mechanism maps: The plasticity and creep of metals and ceramics. <https://engineering.dartmouth.edu/defmech/>. Accessed 8 Feb 2021.
- K. Prasad, R. Sarkar, P. Ghosal, and V. Kumar: *Mater. Des.*, 2010, vol. 31, pp. 4502–507.
- V. Garat, J.M. Cloue, D. Poquillon, and E. Andrieu: *J. Nucl. Mater.*, 2008, vol. 375, pp. 95–101.
- W. Chen and M.C. Chaturvedi: *Mater. Sci. Eng. A*, 1997, vol. 229, pp. 163–68.
- K. Saravanan, V.S.K. Chakravadhanula, S.K. Manwatkar, S.V.S.N. Murty, and P.R. Narayanan: *Metall. Mater. Trans. A*, 2020, vol. 51, pp. 5691–703.
- M.L. Weaver and C.S. Hale: in *Proceedings of the International Symposium on Superalloys and Various Derivatives*, E.A. Loria, ed., vol. 1, The Minerals, Metals and Materials Society, 2001, pp. 421–32.
- B. Max, J.S. Juan, M.L. Nó, J.M. Cloue, B. Viguier, and E. Andrieu: *Metall. Mater. Trans. A*, 2018, vol. 49, pp. 2057–68.
- A. Iturbe, E. Giraud, E. Hormaetxe, A. Garay, G. Germain, K. Ostolaza, and P.J. Arrazola: *Mater. Sci. Eng. A*, 2017, vol. 682, pp. 441–53.
- S.L. Soo, D.K. Aspinwall, and R.C. Dewes: *J. Mater. Process. Technol.*, 2004, vol. 150, pp. 116–23.
- G. Asala, J. Andersson, and O.A. Ojo: *Philos. Mag.*, 2019, vol. 99, pp. 419–37.
- W.S. Lee, C.F. Lin, T.H. Chen, and H.W. Chen: *Mater. Trans.*, 2011, vol. 52, pp. 1734–740.
- W.S. Lee, C.F. Lin, T.H. Chen, and H.W. Chen: *Mater. Sci. Eng. A*, 2011, vol. 528, pp. 6279–286.
- X. Wang, C. Huang, B. Zou, H. Liu, H. Zhu, and J. Wang: *Mater. Sci. Eng. A*, 2013, vol. 580, pp. 385–90.
- W.S. Lee, C.F. Lin, T.H. Chen, and C.S. Huang: *Mater. Trans.*, 2012, vol. 53, pp. 1758–764.
- Y. Bergström: *Mater. Sci. Eng.*, 1970, vol. 5, pp. 193–200.
- Y. Bergström: *Rev. Powder Metall. Phys. Ceram.*, 1983, pp. 79–265.
- U.F. Kocks, A.S. Argon, and M.F. Ashby: *Thermodynamics and Kinetics of Slip*, Pergamon Press, Oxford, 1975.
- H. Mecking and U.F. Kocks: *Acta Metall.*, 1981, vol. 29, pp. 1865–875.
- H. Mecking: in Work hardening in tension and fatigue: proceedings of a symposium, *The Metall. Soc. AIME*, 1977, pp. 67–90.
- Y. Estrin: in *Unified Constitutive Laws of Plastic Deformation*, A.S. Krausz and K. Krausz, eds., Academic Press, 1996, pp. 69–106.
- Y. Estrin and H. Mecking: *Acta Metall.*, 1984, vol. 32, pp. 57–70.
- M. Fisk and A. Lundbäck: *Finite Elem. Anal. Des.*, 2012, vol. 58, pp. 66–73.
- M. Fisk, A. Lundbäck, J. Edberg, and J.M. Zhou: *Finite Elem. Anal. Des.*, 2016, vol. 120, pp. 92–101.
- V. Kalhori, D. Wedberg, and L.E. Lindgren: *Int. J. Mater. Form.*, 2010, vol. 3, pp. 511–14.
- D. Wedberg, A. Svoboda, and L.E. Lindgren: *Model. Simul. Mater. Sci. Eng.*, 2012, vol. 20, 085006.
- L.M. Camus and G. Engberg: *High Temp. Mater. Process.*, 1990, vol. 9, pp. 27–38.
- M. Fisk, J.C. Ion, and L.E. Lindgren: *Comput. Mater. Sci.*, 2014, vol. 82, pp. 531–39.
- A. Malmelöv, M. Fisk, A. Lundbäck, and L. Lindgren: *Materials (Basel)*.
- E. Orowan: *Zeitschrift für Phys.*, 1934, vol. 89, pp. 605–13.
- M. Polanyi: *Zeitschrift für Phys.*, 1934, vol. 89, pp. 660–64.
- G.I. Taylor: *Proc. R. Soc. London A*, 1934, vol. 145, pp. 362–87.
- A. Seeger, J. Diehl, S. Mader, and H. Rebstock: *Philos. Mag.*, 1957, vol. 2, pp. 323–50.
- J.S. Langer:
- G.I. Taylor: *Proc. R. Soc. London A*, 1934, vol. 145, pp. 388–404.
- M. Fukuhara and A. Sanpei: *J. Mater. Sci. Lett.* 1993 1214, 1993, vol. 12, pp. 1122–24.
- L.E. Lindgren, Q. Hao, and D. Wedberg: *Mech. Mater.*, 2017, vol. 108, pp. 68–76.
- H.J. Frost and M.F. Ashby: *Deformation-Mechanism Maps—The Plasticity and Creep of Metals and Ceramics*, Pergamon Press, Oxford, 1982.
- A.H. Cottrell: *Prog. Met. Phys.*, 1953, vol. 4, pp. 205–64.
- G.W. Ardley and A.H. Cottrell: *Proc. R. Soc. Lond. A*, 1953, vol. 219, pp. 328–41.
- A. Van Den Beukel and U.F. Kocks: *Acta Metall.*, 1982, vol. 30, pp. 1027–034.
- J. Cheng, S. Nemat-Nasser, and W. Guo: *Mech. Mater.*, 2001, vol. 33, pp. 603–16.
- A.H. Cottrell and B.A. Bilby: *Proc. Phys. Soc. Sect. A*, 1949, vol. 62, pp. 49–62.
- G. Schoeck: in *Multiscale Phenomena in Plasticity: From Experiments to Phenomenology, Modelling and Materials Engineering*, Springer Netherlands, 2000, pp. 33–56.
- A.S. Agazhanov, D.A. Samoshkin, and Y.M. Kozlovskii: *J. Phys. Conf. Ser.* <https://doi.org/10.1088/1742-6596/1382/1/012175>.
- M. Militzer, W.P. Sun, and J.J. Jonas: *Acta Metall. Mater.*, 1994, vol. 42, pp. 133–41.
- C. Varvenne, G.P.M. Leyson, M. Ghazisaeidi, and W.A. Curtin: *Acta Mater.*, 2017, vol. 124, pp. 660–83.
- G.P.M. Leyson, L.G. Hector, and W.A. Curtin: *Acta Mater.*, 2012, vol. 60, pp. 3873–884.
- G.P.M. Leyson and W.A. Curtin: *Model. Simul. Mater. Sci. Eng.*, 2016, vol. 24, 065005.
- R. Labusch: *Phys. Status Solidi*, 1970, vol. 41, pp. 659–69.
- A. Argon: *Strengthening Mechanisms in Crystal Plasticity*, Oxford University Press, Oxford, 2007.
- R.L. Fleischer: *Acta Metall.*, 1963, vol. 11, pp. 203–09.
- Y. Mishima, S. Ochiai, N. Hamao, M. Yodogawa, and T. Suzuki: *Trans. Japan Inst. Met.*, 1986, vol. 27, pp. 648–55.
- H. Kou, W. Li, J. Ma, J. Shao, Y. Tao, X. Zhang, P. Geng, Y. Deng, Y. Li, X. Zhang, and F. Peng: *Int. J. Mech. Sci.*, 2018, vol. 140, pp. 83–92.
- R. Kapoor and S. Nemat-Nasser: *Mech. Mater.*, 1998, vol. 27, pp. 1–2.
- D.L. Holt: *J. Appl. Phys.*, 1970, vol. 41, pp. 3197–201.
- E.I. Galindo-Nava and P.E.J. Rivera-Díaz-Del-Castillo: *Int. J. Plast.*, 2013, vol. 47, pp. 202–21.
- S. Azadian: Luleå University of Technology, 2004.
- M.A. Moretti, B. Dalai, P. Åkerström, C. Arvieu, D. Jacquin, E. Lacoste, and L.-E. Lindgren: *Metall. Mater. Trans. A*, 2021, pp. 1–15.
- C.L. Hale, W.S. Rollings, and M.L. Weaver: *Mater. Sci. Eng. A*, 2001, vol. 300, pp. 153–64.
- S.A. Nalawade, M. Sundararaman, R. Kishore, and J.G. Shah: *Scr. Mater.*, 2008, vol. 59, pp. 991–94.
- M.C. Rezende, L.S. Araújo, S.B. Gabriel, J. Dille, and L.H. De Almeida: *J. Alloys Compd.*, 2015, vol. 643, pp. S256–59.
- G.Z. Voyiadjis and Y. Song: *Acta Mech.*, 2020, vol. 231, pp. 19–34.
- K. Yuan, W. Guo, P. Li, J. Wang, Y. Su, X. Lin, and Y. Li: *Mater. Sci. Eng. A*, 2018, vol. 721, pp. 215–25.
- M. Azarbarmas, M. Aghaie-Khafri, J.M. Cabrera, and J. Calvo: *Mater. Des.*, 2016, vol. 94, pp. 28–38.
- M. Azarbarmas, M. Aghaie-Khafri, J.M. Cabrera, and J. Calvo: *Mater. Sci. Eng. A*, 2016, vol. 678, pp. 137–52.
- Y. Wang, W.Z. Shao, L. Zhen, L. Yang, and X.M. Zhang: *Mater. Sci. Eng. A*, 2008, vol. 497, pp. 479–86.

67. F. Montheillet and J.-P. Thomas: in *Metallic Materials with High Structural Efficiency*, O.N. Senkov, D.B. Miracle, and S.A. Firstov, eds., Kluwer Academic Publishers, **Dordrecht**, 2004, pp. 357–68.
68. F.L. Sui, L.X. Xu, L.Q. Chen, and X.H. Liu: *J. Mater. Process. Technol.*, 2011, vol. 211, pp. 433–40.
69. Y.B. Tan, Y.H. Ma, and F. Zhao: *J. Alloys Compd.*, 2018, vol. 741, pp. 85–96.
70. F. Chen, J. Liu, H. Ou, B. Lu, Z. Cui, and H. Long: *Mater. Sci. Eng. A*, 2015, vol. 642, pp. 279–87.
71. J.P. Thomas, E. Bauchet, C. Dumont, and F. Montheillet: in *Proceedings of the International Symposium on Superalloys*, 2004.
72. A. Akhtar and E. Teghtsoonian: *Metall. Trans.*, 1971, vol. 2, pp. 2757–63.
73. Y. Mishima, S. Ochiai, and T. Suzuki: *Acta Metall.*, 1985, vol. 33, pp. 1161–69.
74. L. Karmazin: *Czechoslov. J. Phys.* 1979, vol. 29.
75. Y. Mishima, S. Ochiai, N. Hamao, M. Yodogawa, and T. Suzuki: *Trans. Jpn. Inst. Met.*, 1986, vol. 27, pp. 656–64.
76. A.S. Argon: *Physical Metallurgy*, Elsevier, Amsterdam, 1996, pp. 1877–955.
77. A.S. Argon: *Scr. Metall.*, 1970, vol. 4, pp. 1001–1004.
78. W.P. Kuykendall, Y. Wang, and W. Cai: *J. Mech. Phys. Solids*, 2020, vol. 144, 104105.
79. L.P. Kubin, G. Canova, M. Condat, B. Devincre, V. Pontikis, and Y. Bréchet: *Solid State Phenom.*, 1992, vol. 23–24, pp. 455–72.
80. A. Malka-Markovitz and D. Mordehai: *Philos. Mag.*, 2018, vol. 98, pp. 347–70.
81. M.J. Sohrabi and H. Mirzadeh: *Vacuum*. <https://doi.org/10.1016/j.vacuum.2019.108875>.
82. M.J. Sohrabi and H. Mirzadeh: *Met. Mater. Int.*, 2020, vol. 26, pp. 326–32.
83. D. Connétable, B. Ter-Ovanesian, and É. Andrieu: *J. Phys. Condens. Matter*, 2012, vol. 24, pp. 1–5.
84. Y. Han and M.C. Chaturvedi: *Mater. Sci. Eng.*, 1987, vol. 85, pp. 59–65.
85. X. Feaugas and H. Haddou: *Metall. Mater. Trans. A*, 2003, vol. 34A, pp. 2329–40.
86. M. Sundararaman, P. Mukhopadhyay, and S. Banerjee: *Acta Metall.*, 1988, vol. 36, pp. 847–64.
87. Phonon density of states of the Debye model. <https://lampx.tugraz.at/~hadley/ssl/phonons/table/dosdebye.html>. Accessed 22 Apr 2022.
88. Special Metals Corporation - Inconel alloy 718. <https://www.specialmetals.com/documents/technical-bulletins/inconel/inconel-alloy-718.pdf>. Accessed 27 Nov 2018.

Publisher's Note Springer Nature remains neutral with regard to jurisdictional claims in published maps and institutional affiliations.